Characterization of the Tidal Resource in Rathlin Sound

Alberto Pérez-Ortiz[a1], Alistair G. L. Borthwick[b], James McNaughton[c], Alexandros Avdis[d]

a Industrial Doctoral Centre for Offshore Renewable Energy. School of Engineering, The University of Edinburgh, The King's Buildings, Edinburgh, EH9 3JL, UK.
b Institute of Energy Systems, School of Engineering, The University of Edinburgh, The King's Buildings, Edinburgh, EH9 3JL, UK.
c General Electric Renewable Energy. 214 Castlemead, Lower Castle Street, Bristol, BS1 3AG, UK.
d Applied Modelling and Computation Group, Department of Earth Science and Engineering, Imperial College London, London, SW7 2AZ, UK.

Abstract

Tidal resource assessment is presented for Rathlin Sound, located between Rathlin Island and the north-east coast of Northern Ireland. The flow is simulated in 2D, using the shallow water equations. For an M_2 tide, the natural flow conditions exhibit local spatial mean and maximum flow speeds of 2 and 3 m/s. Upper limits to power extraction are about 298 MW for M_2 and 330 MW for M_2+S_2 tidal signals (different to undisturbed kinetic power and power naturally dissipated at the seabed). An analytical model of a channel connecting two infinite ocean basins underpredicts maximum power extracted in Rathlin Sound due to changes in head driving the flow and the existence of an alternative flow path. At maximum power extracted, there is substantial reduction in mean flow speeds in the strait and to the south-east of Rathlin Sound. In the strait, maximum power is reduced by 14 % and 36 % for blockage ratios of 80 % and 60 %. Power extraction both offshore of the island and in the strait yields higher power generation rates than isolated extraction. Resource assessments for Rathlin Sound are generally in good agreement with those for an idealised strait between an island and landmass.

Keywords

Tidal Energy; Resource Assessment; Numerical Modelling; Strait; Island; Landmass

[1] Corresponding author.
Present address: Suspro, 1 Diamond Street, Bristol, BS3 3LF, UK.
E-mail address: alberto.perez@suspro.net

1 Introduction

Renewable energy technologies are of increasing importance as likely mitigation measures against climate change [1] and the finiteness of fossil fuel resources [2]. Of such technologies, tidal stream energy possesses the advantages of being almost entirely deterministic, unlike wind or solar energy, and having locally high energy density which limits the footprint of tidal projects [3], [4]. Determination of tidal resource and the environmental implications of large-scale tidal energy exploitation is nevertheless subject to large uncertainty arising from model limitations, site data measurement errors, the presence of gravity waves and turbulence, etc. [5], [6], [7]. Moreover, bed friction is often used as a tuning parameter and this can lead to errors in the results related to the availability and accuracy of site-specific calibration data [8]. To date, assessment of tidal resource has been analysed through two approaches: analytical and numerical analyses of idealised tidal sites [9] [10]; and numerical analysis of actual tidal sites [11]. Draper [12] suggested a possible classification of generic coastal sites suitable for tidal stream energy exploitation: a channel linking two infinite ocean basins; a channel linking an infinite ocean basin and an enclosed bay; a headland; and a strait between an island and a landmass. The analytical channel model derived by Garrett and Cummins (GC2005) [9] provides theoretical limits to power extraction in a channel linking two infinite ocean basins and also at a strait between an island and a landmass. The GC2005 model assumes that the head driving the flow in the channel does not change with power extraction, and that flow cannot divert from the channel. Under these assumptions, the GC2005 model computes the maximum average power available for extraction, based on the head driving the flow, the maximum volumetric flow rate through the channel, and the phase difference between the driving head and flow in the channel.

Pérez-Ortiz *et al*. [13], [14] used a numerical solver of the shallow water equations to examine the validity of the GC2005 model in identifying the upper limit to power extraction for an idealised strait between an island (of various aspect ratios) near a landmass and for an isolated offshore island forced exclusively with an M_2 tidal signal. The idealised island-landmass model [13], [14] comprised an ellipsoidal obstacle representing the island situated in a coastal domain with open boundaries at its west and east ends, and solid walls along the north and south boundaries; the model was run for a total of 7 tidal cycles, two for ramp-up, three for spin-up, and the final three for resource assessment. In [13], [14], the presence of tidal turbines was included through enhanced bed friction, following the approach originally suggested by Sutherland *et al*. [15] and Karsten *et al*. [16]. The GC2005 model was shown to give very satisfactory results for long islands extending parallel to the landmass, but tended to under-predict the maximum power extracted in the strait for short islands. The agreement observed for long islands is due to the insignificant changes in the head drop along the strait with power extraction, and minimal bypass flow offshore of the island. Pérez-Ortiz *et al*.[13], [14] compared the maximum extracted power to the undisturbed kinetic power and the natural power dissipated at the seabed in the strait; parameters that have been used in the past to assess the resource at tidal sites [17]. Except for the case of an island extending parallel to a landmass, where the numerically predicted extracted power is satisfactorily approximated by the power naturally dissipated at the seabed, no clear relationship was found between the maximum extracted power and the undisturbed kinetic power or the natural power dissipated at the seabed in the strait. In addition, the analysis assessed the effects on the limits to power extraction at the coastal site to the choice of numerically specified bottom friction and eddy viscosity, offshore bathymetry, strait blockage, and combined power extraction in the strait and offshore of the island.

Several actual coastal sites that could fall into the category of a strait between an island and a landmass have previously been investigated. The extractable power of the Pentland Firth, a strait located between the north coast of Scotland and the Orkney Islands, was assessed by Adcock *et al*. [18] and Draper *et al.* [11]. Extracted power estimates by Draper *et al*. [11] are in good agreement with the predictions by GC2005. Close agreement between the numerical and GC2005 limits to power extraction was also found by Sutherland *et al*. [15] for the Johnstone Strait, located between Vancouver Island and the west coast of Canada. At both tidal stream sites, the island extends a long distance along the coast, and so, according to Pérez-Ortiz *et al*. [13] the GC2005 model is well within its range of applicability.

This paper presents a resource assessment of the Rathlin Sound coastal site, and assesses the validity of the idealised island-landmass approximation by Pérez-Ortiz *et al*. [13] and GC2005 analytical channel model when applied to an actual site of similar island and strait aspect ratios. Rathlin Sound is an energetic tidal site delimited by Rathlin Island and the north-east coast of Northern Ireland, and located within the North Channel between Ireland and Scotland (Figure 1). Rathlin Island is about 7.5 km long, and its width ranges from 2 km at its centre and west side to 6 km south to Rue Point at the east side. The breadth of Rathlin Sound ranges from 4 km to 10 km, i.e. of the same order as the length and width of the island. Mean water depths in the strait and offshore of Rathlin Island are 60 m and 180 m respectively. The coast of Northern Ireland possesses three headlands that influence the flow dynamics at Rathlin Sound: Fair Head, located east of the Rathlin Sound; Torr Head, located south-east of Rathlin Sound; and Kimbane Head, located west of Rathlin Sound. Two interacting tidal flows, one progressing north from the Irish Sea through the North Channel east of Rathlin Sound and a second tide progressing east from the Atlantic, are the primary drivers of flow dynamics within the Rathlin Sound. These result in currents flowing from west to east during flood tide and from east to west during ebb tide. O'Rourke *et al*. [19] have estimated the potential power generation to be slightly over 100 GWh/year off the north east coast of Ireland, including Rathlin Sound and sites off Fair Head headland east from Rathlin Island. Lewis *et al*. [3] assessed numerically the undisturbed tidal stream resource that is hydrodynamically available in the Irish Sea, including the Rathlin Sound, and analysed its dependence on operating water depths and current velocities for present and future tidal technologies.

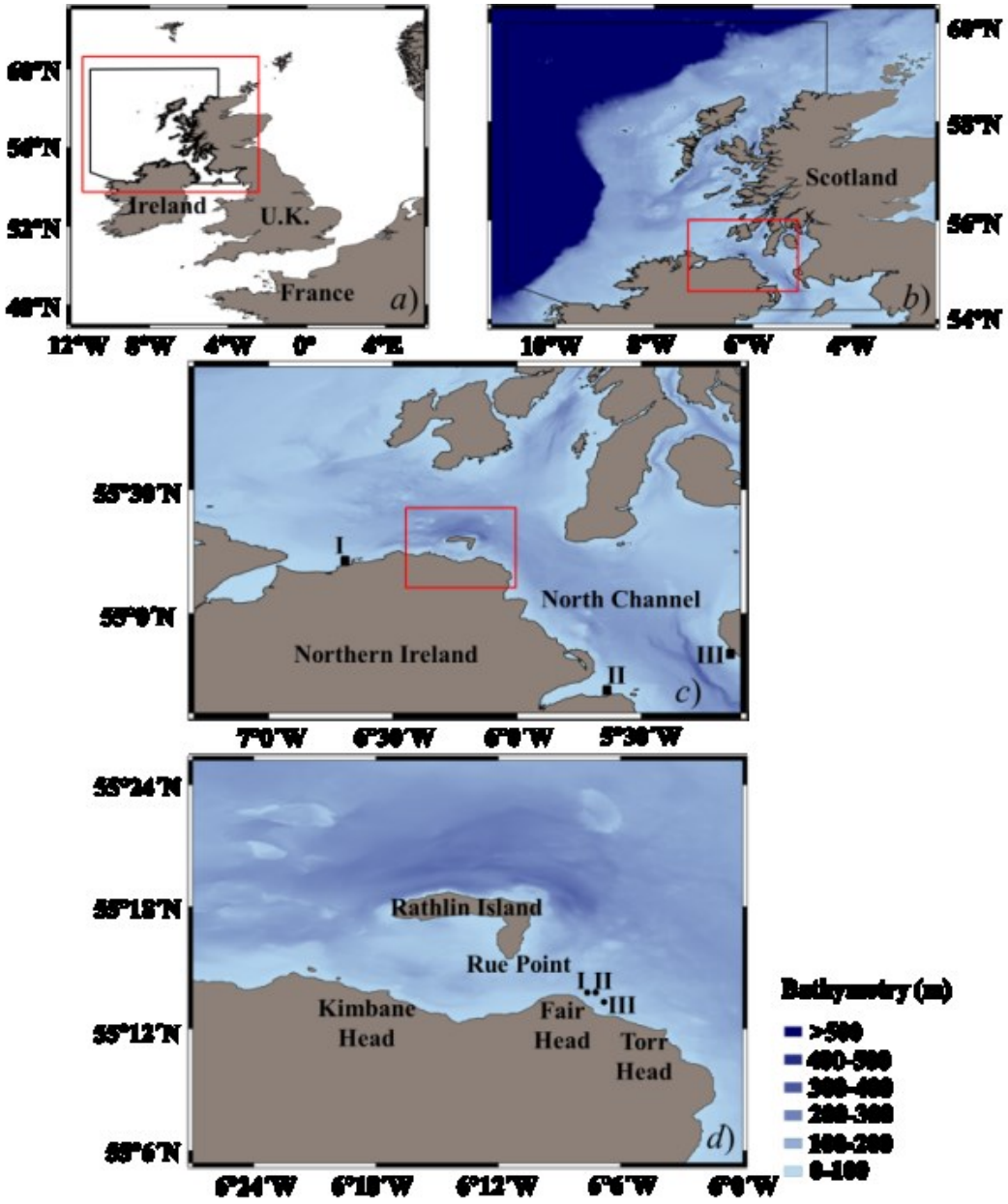

Figure 1. (a) Overview of Rathlin domain relative to the British Isles; (b) bathymetry with respect to mean sea level vertical reference datum for the Rathlin domain; and (c) close-up plan views of the bathymetry and (d) coastal features at the Rathlin Sound [20]. Red boxes indicate areas covered by the close-up views. Tidal gauge locations (square): I) Portrush; II) Bangor; and III) Portpatrick. ADCP locations (circle): I) ADCP 1; II) ADCP 2; and III) ADCP 3.

The paper is structured in four sections. Section 2 describes the underlying methodology and set-up of the Rathlin Sound numerical model. Section 3 describes the natural flow conditions at Rathlin Sound in the absence of power extraction. Section 4 details the resource assessment of Rathlin Sound and the associated environmental effects, and compares them against the results from the idealised island-landmass study. Section 5 lists the conclusions.

2 Methodology

2.1 Numerical Model Parameterization

Tidal simulations are undertaken using the finite element code Fluidity [21] which solves the non-conservative form of the shallow water equations:

$$\frac{\partial \eta}{\partial t} + \nabla \cdot (h\bar{u}) = 0 \quad (1)$$

$$\frac{\partial \bar{u}}{\partial t} + \bar{u} \cdot \nabla \bar{u} + g\nabla\eta + C_d \frac{|\bar{u}|\bar{u}}{h} = 0 \quad (2)$$

where η is the free surface elevation above mean water level, $\bar{u}$ is the horizontal velocity vector, t is time, ∇ is the horizontal gradient vector, h is the total water depth, g is the gravitational acceleration, and C_d is the non-dimensional bottom drag coefficient. The model setup is based on Pérez-Ortiz *et al*. [13] following guidelines for coastal and tidal power extraction modelling provided by the Fluidity developers [22] [23]. A $P_{1DG}P_2$ mixed finite element discretization scheme is employed, which is linear discontinuous Galerkin for velocity and quadratic continuous Galerkin for pressure. The momentum equation is temporally discretised using the backward Euler scheme [24]. A Generalised Minimal Residual Method (GMRES) solver with a Successive Over-Relaxation (SOR) pre-conditioner [22] is employed to resolve both velocity and pressure fields. The tolerance in the absolute error solution and the maximum number of iterations are specified as 10^{-7} and 1,000 respectively for both velocity and pressure fields. Viscosity is implemented by means of a depth averaged parabolic eddy viscosity empirical model [25]:

$$\nu_t = \frac{k}{6}[C_d(u^2+v^2)]^{1/2}h \quad (3)$$

where k = 0.41 is the von Kármán constant, and u and v are the depth-averaged velocity components. Wetting and drying is not implemented in the model because the length scale of the inter-tidal regions is relatively small compared to the model resolution and domain extension. Nevertheless, a minimum depth of 5 m is prescribed in the domain to avoid numerical instabilities at areas of the domain with high tidal ranges. Coriolis effects are uniform across the domain and computed from:

$$f = 2\Omega \sin\lambda \quad (4)$$

where Ω is the frequency of the Earth's rotation, and λ is the latitude of the Rathlin Sound, taken as 55.25 ^{o}N. Other site-dependent parameters such as atmospheric pressure, wind, or wave conditions are not included in the numerical model. The time step is set at 60 s to limit the Courant-Friedrichs-Lewy number to be within O(1).

The presence of turbines is included in the model through addition of an equivalent seabed friction coefficient k_f, or extraction level, over the footprint area of the array A_f [11], [15], [16]. The extraction level k_f is defined as follows:

$$k_f = \frac{N_T(C_T A_T + C_D A_S)}{2A_f} \quad (5)$$

where N_T is the equivalent number of turbines, A_T is the turbine rotor projected area; A_S is the turbine support structure projected area (A_S = 0.1A_T); and C_T and C_D are the thrust and drag turbine coefficients (assumed constant and equal to 0.8 and 0.9 respectively) [26]. Here the turbines are assumed to have 20 m rotor diameter and a power rating, P_R, equal to 1 MW. The

power is then determined by integrating the bed friction over the footprint area, and multiplying by the ratio of the additional bed friction coefficient (representing the added turbines) to the total bed friction coefficient (representing natural conditions and added turbines) following the approach proposed by Sutherland *et al*. [15]. The additional bed friction coefficient is varied systematically, and the peak power determined. This methodology of power extraction is unable to account for mixing losses at turbine-scale, and so the results represent an upper limit to power extraction [27].

Figure 2 shows the limits and coastlines of the numerical domain, located within longitudes 3.5 – 11 °W and latitudes 54.2 – 60 °N. The domain extends to the edge of the continental shelf, so that the deep water zone attenuates reflected long waves from the coastlines and power extraction zone, before reaching open boundaries [28]. The numerical domain has two solid boundaries defined by the coastlines of Ireland and the United Kingdom and two open boundaries located south-east and north-west of the domain. The domain coastlines were derived from the zero-depth contour of the bathymetry (Figure 1) in the near-field region. In the far-field region, where the precise detail of the coastline is not likely to affect hydrodynamics at the site, coastlines were obtained from the GSSHG NOAA database [20] at approximately 100 m spatial resolution in Mean Sea Level (MSL) vertical datum.

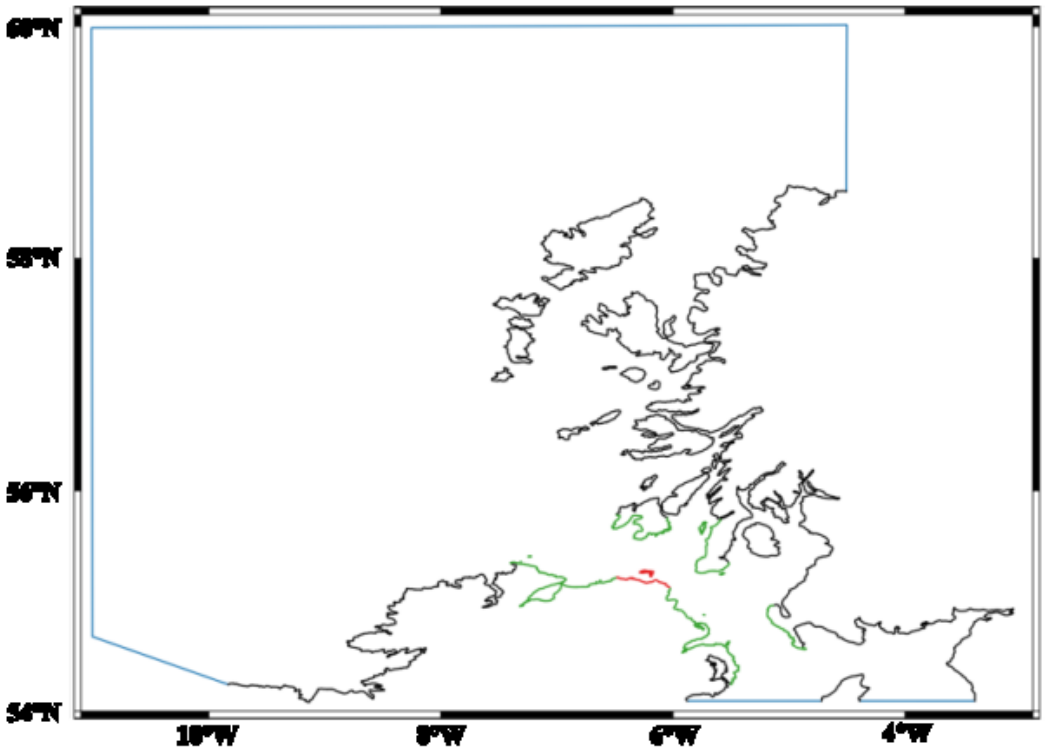

Figure 2. Computational domain boundaries, coastlines and mesh regions: open boundaries (blue); mesh regions 1 (red); 2 (green); and 3 (black).

Site bathymetry data obtained from the HydroSpatial One Gridded Bathymetry dataset [20] were converted from lowest astronomical tide (LAT) to the mean sea level (MSL) vertical datum using the Vertical Offshore Reference Frame (VORF) model available for British and Irish waters [29]. Two bathymetry data resolutions were used: 1 arcsec for the area contained within longitude and latitude coordinates 4 – 8 °W and 54 – 56 °N; and 6 arcsec throughout the rest of the domain. Due to the difference in resolution between VORF, 28.8 arcsec, and the bathymetry

used, nearest-point interpolation was used to modify the vertical reference of the bathymetry data. All datasets were in WGS84 geographic horizontal datum.

Sea surface elevation conditions at the open boundaries are derived from the Oregon State University European shelf model [30]. The tidal signal is ramped up over 24 hours using the following amplitude multiplier:

$$a_o = 0.5\left(1 - \cos\left(\frac{\omega_t t}{4}\right)\right) \quad 6)$$

where ω_t is equal to 7.27 x 10^{-5} rad/s. A further spin-up period of 48 hours is implemented to allow the system to stabilise

2.2 Spatial Discretization and Mesh Convergence

The shorelines and open boundaries depicted in Figure 2 were also selected to facilitate mesh generation. The domain geometry (coastlines and domain boundaries) and mesh size distribution are defined in the open-source Geographic Information System QGIS [31] and imported into the mesh generator Gmsh [32] using qmesh [33]. Given the proximity of the proposed tidal farm to shorelines, a mesh gradating to smaller elements close to shorelines was employed to discretise spatially the domain. The regions identified in Figure 2 were therefore chosen to distribute optimally the element edge length throughout the domain: In the region of interest (region 1) the mesh features the smallest elements in order to represent the flow dynamics as accurately as possible, whereas in Region 2 and Region 3 the mesh gradates to larger cell sizes in order to capture correctly the flow in the surrounding area. Four meshes were constructed in order to examine the sensitivity and convergence of the results, as summarised in Table I. The exact variation of the element edge length was described in terms of the distance to the closest shoreline, or proximity functions [33], [34]. The proximity function is mapped to a mesh edge length distribution satisfying the following metrics: A constant edge length is maintained over a distance corresponding to 0.15 degrees from the closest coastline, and then linearly increases to a specified edge length over a distance corresponding to 1 degree. The defined mesh edge length determines the minimum size of the islands and bays that are spatially captured by the grid in the far-field region. Finally, the mesh is generated in the UTM29 zone, the conversion of domain geometry and element edge length is automated by qmesh. Mesh generation and pre-processing of domain coastlines, including deletion of small islands and closure of small shallow bays, are iteratively executed until a satisfactory mesh is achieved.

Table I. Four spatial discretization cases considered in the mesh convergence analysis: the table lists the element edge length used at the three coastlines and offshore, and the total number of mesh elements.

	Mesh element edge length (m)				
Mesh	Coast 1	Coast 2	Coast 3	Offshore	Mesh elements
1	1000	2000	10000	100000	11,708
2	500	1000	5000	50000	40,152
3	250	500	2500	25000	147,750
4	125	250	1250	12500	569,906

For the mesh sensitivity analysis, the model is forced solely by an M_2 tidal signal at the open boundaries, and solution convergence assessed at four transects which extend north of the coast of Northern Ireland until latitude coordinate 55.375 ^{o}N: two transects at the west (2) and east (3) ends of Rathlin Sound, and two transects 10 km downstream from the west (1) and east (4) ends of Rathlin Sound. Figure 3 presents the flow speed, computed as $|U| = (u^2 + v^2)^{1/2}$, at peak flow during ebb and flood tide at the four transects for the four mesh cases of Table I. Mesh convergence appears to have been almost achieved for Mesh 3. However, the solution has not fully converged in Transects 1 and 4 at ebb tide and flood tide respectively, showing that further refinement may be necessary to capture advective flow features generated at the island. Mesh 3 captures the main flow features generated at the island and in the strait, and so is employed in this analysis as it is considered to provide sufficient accuracy for the purposes of resource assessment in the strait. Figure 4 provides an overview of the mesh, showing local refinement in the area of interest. The open boundaries do not exactly follow the corresponding lines shown in figure 2, as Gmsh fits a bspline through the corner points [34]. This was nonetheless found to produce a satisfactory domain representation.

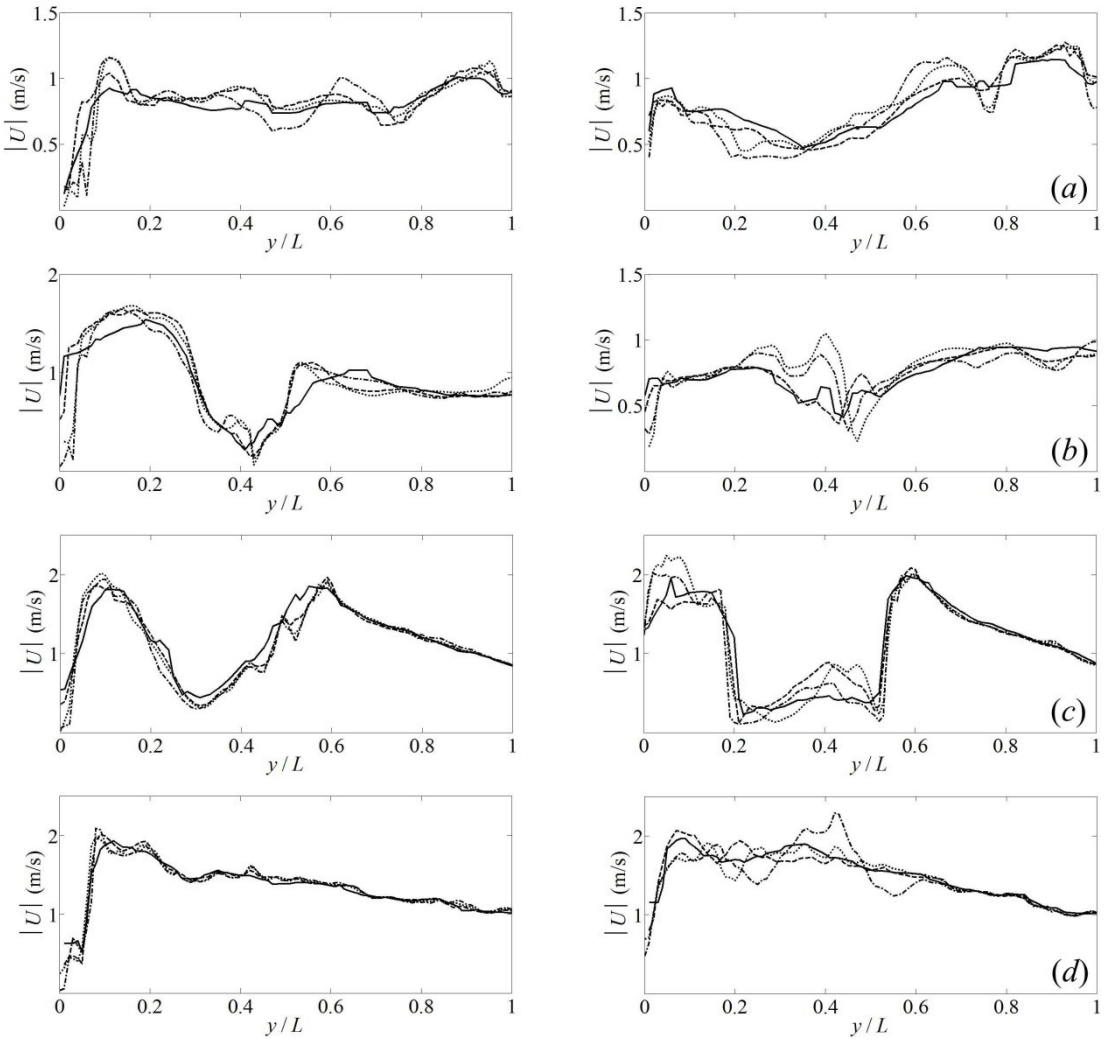

Figure 3. Depth-averaged flow speed distributions at peak flow during ebb tide (left column) and flood tide (right column) at (*a*) Transect 1; (*b*) Transect 2; (*c*) Transect 3; and (*d*) Transect 4. Mesh 1 (solid line); Mesh 2 (dashed line); Mesh 3 (dotted line); and Mesh 4 (dash-dot line).

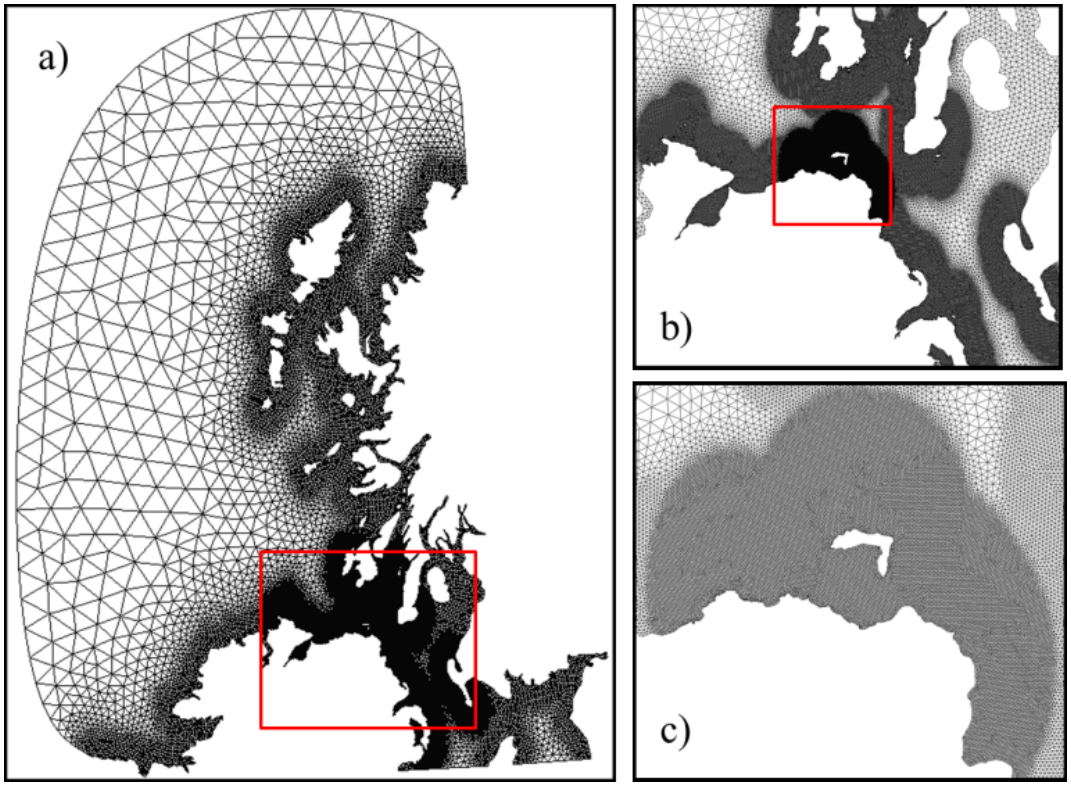

Figure 4. Spatial discretization of the domain: Mesh 3: (a) total mesh domain, (b) sub-domain mesh in North Channel between Ireland and Scotland, (c) close-up of local mesh resolution in the vicinity of Rathlin Sound. Red squares indicate the domain area zoomed in.

2.3 Calibration of the Numerical Model

Two datasets of field observations are used for calibration of the numerical model: free surface elevation and depth-averaged flow velocity data averaged over 10-minute intervals from three ADCPs deployed by DP Marine Energy Ltd [35] south-east of Rathlin Sound (Figure 1 and Table II); and sea surface elevation data from three UK tidal gauge stations provided by the British Oceanographic Data Centre [36] (Figure 1 and Table III). The tidal gauge stations are: Portrush, off the north coast of Northern Ireland, west of Rathlin Sound; Bangor, in Belfast Lough north-east of Belfast, south-east of Rathlin Sound; and Portpatrick, on the east side of the North Channel, south-west Scotland, south-east of Rathlin Sound.

Table II. Latitude and longitude coordinates of deployed ADCPs, and sampling durations [35].

ADCP	Latitude (deg)	Longitude (deg)	Sampling time period (Start – End)
1	55.230 N	6.114 W	24/04/2014 – 27/05/2014
2	55.228 N	6.113 W	24/04/2014 – 04/06/2014
3	55.222 N	6.090 W	24/04/2014 – 04/06/2014

Table III. Latitude and longitude coordinates and sampling durations for data collected at the three UK tidal gauge stations in the proximity of Rathlin Sound [36].

Station	Latitude (deg)	Longitude (deg)	Time period data (Start – End)
Portrush	55.207 N	6.657 N	27/04/2014 – 28/05/2014
Bangor	54.665 N	5.669 N	27/04/2014 – 28/05/2014
Portpatrick	54.843 N	5.120 N	27/04/2014 – 28/05/2014

For the calibration process, the model is forced with 8 harmonic constituents, M_2, S_2, N_2, K_2, K_1, O_1, P_1, and Q_1, for 18 days starting on 24th April 2014. The first three days of the simulation correspond to the ramp-up and spin-up of the system; results from the following 15 days covering a spring-neap tidal cycle are used for calibration purposes. The calibration of the numerical model is performed by altering the seabed friction coefficient, C_d, throughout the domain, for values in the range between 0.001 and 0.005 [37]. For this range of seabed friction coefficients, Table IV and Table V compare respectively the normalised measured and computed M_2 and S_2 free surface amplitudes and phases for the ADCP and tidal gauge stations. In both cases, values of harmonic constituents are obtained with the Matlab based tool T_Tide [38]. Results in Table IV show that amplitude and phase of the M_2 free surface elevation are best approximated by setting C_d = 0.0025 or 0.003 at the three ADCP locations. At Portrush, these seabed friction coefficients yield a satisfactory approximation to the M_2 phase, but the amplitude is better approximated using lower seabed friction coefficients. M_2 free surface amplitude at Bangor appears to be independent of the seabed friction coefficient and agreement in phase decreases with seabed friction coefficient. At Portpatrick, the increase in seabed friction coefficient yields improved agreement in amplitude. Close agreement is obtained using C_d = 0.0025 or 0.003 for predicted S_2 free surface amplitude at the ADCP locations, although the S_2 phase is not so well captured by the numerical model. S_2 amplitude and phase at Portrush, Bangor and Portpatrick are relatively well reproduced, albeit no clear relationship is observed between the numerical results and choice of seabed friction coefficient.

Table IV. Comparison of normalised measured and Fluidity predicted M_2 free surface amplitudes $A^* = A_{computed} / A_{measured}$ and phases $\phi^* = \phi_{computed} - \phi_{measured}$ (deg) for the ADCP and tidal gauge stations for seabed friction coefficients C_d in the range from 0.001 to 0.005.

Location	Model Magnitude											
	C_d = 0.001		C_d = 0.002		C_d = 0.0025		C_d = 0.003		C_d = 0.004		C_d = 0.005	
	A^*	ϕ^*	A^*	ϕ^*	A^*	ϕ^*	A^*	ϕ^*	A^*	ϕ^*	A^*	ϕ^*
ADCP 1	1.10	-10.40	1.03	-3.80	1.03	-0.80	1.00	2.30	0.97	8.50	0.97	14.30
ADCP 2	1.07	-9.40	1.03	-3.00	1.00	0.00	0.97	3.10	0.93	9.10	0.93	14.90
ADCP 3	1.15	-3.60	1.09	2.20	1.06	5.00	1.03	8.00	0.97	14.00	0.94	19.90
Portrush	1.04	3.60	0.96	1.60	0.94	0.20	0.90	-1.20	0.84	-3.90	0.80	-6.50
Bangor	0.96	-1.10	0.96	0.50	0.96	1.20	0.96	2.00	0.95	3.60	0.95	5.10
Portpatrick	0.92	1.00	0.95	1.20	0.96	1.30	0.97	1.50	0.98	1.80	0.99	2.10

Table V. Comparison of normalised measured and Fluidity predicted S_2 free surface amplitudes $A^* = A_{computed} / A_{measured}$ and phases $\phi^* = \phi_{computed} - \phi_{measured}$ (deg) for the ADCP and tidal gauge stations for seabed friction coefficients C_d in the range from 0.001 to 0.005.

Location	Model Magnitude											
	C_d = 0.001		C_d = 0.002		C_d = 0.0025		C_d = 0.003		C_d = 0.004		C_d = 0.005	
	A^*	ϕ^*	A^*	ϕ^*	A^*	ϕ^*	A^*	ϕ^*	A^*	ϕ^*	A^*	ϕ^*
ADCP 1	4.00	64.90	3.00	58.40	2.00	50.70	1.00	31.70	1.00	-32.50	1.00	-75.50
ADCP 2	4.00	68.40	2.00	62.70	2.00	55.20	1.00	30.60	1.00	-60.10	2.00	-89.70
ADCP 3	2.33	9.20	1.67	14.00	1.33	18.40	1.00	26.80	0.33	65.80	0.67	116.70
Portrush	1.09	0.60	1.04	-2.80	1.04	-4.50	1.04	-6.30	1.00	-9.40	0.96	-12.10
Bangor	1.07	-10.00	1.07	-7.50	1.07	-6.30	1.07	-5.10	1.07	-2.70	1.07	-0.40
Portpatrick	1.03	-5.60	1.05	-5.90	1.08	-5.90	1.08	-5.80	1.11	-5.70	1.11	-5.50

Table VI and Table VII compare respectively the normalised measured and computed M_2 and S_2 flow velocities at the ADCP locations for seabed friction coefficients between 0.001 and 0.005. At the three ADCP locations, the M_2 major ellipses are best approximated by C_d = 0.002, showing that the model is able to capture well the magnitude of the stream-wise velocity component. The M_2 minor ellipse is better approximated for low C_d. Transverse velocity component predictions are not as accurate as those obtained for the stream-wise component, but an order of magnitude lower than the stream-wise component. The M_2 phase is reasonably well captured at ADCP 1 and 2 using C_d = 0.0025. Higher C_d is required to improve agreement with the measured data at ADCP 3. The change in C_d does not appear to have an effect on the M_2 inclination, revealing that this may be a bathymetry-dependent parameter which can only be better resolved by further local mesh refinement. The S_2 major and minor ellipses, phase and inclination follow similar trends to those observed in the M_2.

Table VI. Comparison of normalised measured and computed M_2 currents at the ADCP locations for different seabed friction coefficients C_d in the range from 0.001 to 0.005.

Location	Model magnitude					
	C_d = 0.001	C_d = 0.002	C_d = 0.0025	C_d = 0.003	C_d = 0.004	C_d = 0.005
Major ellipse parameter: $C_{max\_computed}$ / $C_{max\_measured}$						
ADCP 1	1.11	0.99	0.95	0.91	0.84	0.78
ADCP 2	1.06	0.95	0.91	0.86	0.80	0.75
ADCP 3	1.09	0.98	0.93	0.89	0.81	0.76
Minor ellipse parameter: $C_{min\_computed}$ / $C_{min\_measured}$						
ADCP 1	0.13	0.20	0.20	0.20	0.07	-0.07
ADCP 2	0.22	0.28	0.22	0.22	0.11	0.06
ADCP3	2.00	1.25	1.25	1.00	1.00	0.75
Phase: $\phi_{computed}$ - $\phi_{measured}$ (deg)						
ADCP 1	-19.1	-6.4	-1.4	1.4	2.3	1.2
ADCP 2	-15.9	-4.9	0.2	3.6	6.2	5.7
ADCP3	-45.8	-38.2	-31.5	-32.1	-33.6	-27.7
Inclination: $\theta_{computed} - \theta_{measured}$ (deg)						
ADCP 1	-9.9	-10	-10.1	-10.4	-11	-11.5
ADCP 2	-8.1	-8.3	-8.5	-8.9	-9.6	-10.2
ADCP3	2.1	1.3	1.4	1.1	0.9	0.6

Table VII. Comparison of normalised measured and computed S_2 currents at the ADCP locations for a range of seabed friction coefficients 0.001-0.005.

Location	Model magnitude					
	C_d = 0.001	C_d = 0.002	C_d = 0.0025	C_d = 0.003	C_d = 0.004	C_d = 0.005
Major ellipse parameter: $C_{max\_computed}$ / $C_{max\_measured}$						
ADCP 1	1.21	1.08	1.00	0.97	0.86	0.78
ADCP 2	1.12	1.01	0.94	0.91	0.81	0.73
ADCP 3	1.21	1.10	1.01	0.96	0.85	0.78
Minor ellipse parameter: $C_{min\_computed}$ / $C_{min\_measured}$						
ADCP 1	0.50	0.42	0.33	0.25	0.08	0.08
ADCP 2	0.54	0.46	0.38	0.31	0.15	0.08
ADCP3	0.57	0.29	0.14	0.14	0.14	0.14
Phase: $\phi_{computed}$ - $\phi_{measured}$ (deg)						
ADCP 1	-46	-23.4	-17.9	-9	-3.8	-4.7
ADCP 2	-40.3	-19.7	-13.4	-4.6	3.3	4
ADCP3	-97.9	-91.8	-98.7	-98.9	-106.1	-100.7
Inclination: $\theta_{computed} - \theta_{measured}$ (deg)						
ADCP 1	-8.1	-8.3	-8.9	-9.1	-10.2	-11.2
ADCP 2	-7.2	-7.3	-8.1	-8.4	-9.8	-10.7
ADCP3	1.1	0.7	0.2	0.7	0.3	0.5

The calibration test results indicate that the measured free surface and velocity data in the vicinity and far-field of the site are best reproduced using a seabed friction coefficient C_d = 0.0025. For validation, the model is then rerun for a further 33 days starting on 9th May 2014, for C_d = 0.0025 and 8 harmonic constituents.

Table VIII presents the coefficient of determination R^2 computed at the three ADCP locations for the stream-wise and transverse velocity components respectively, for 15 days starting on the 12th of May 2014.

Table VIII. Coefficient of determination R^2 for the stream-wise u and v velocity components at ADCP 1, 2 and 3 locations, for seabed friction C_d = 0.0025.

Location	u	v
ADCP 1	0.97	0.72
ADCP 2	0.96	0.82
ADCP 3	0.96	0.96

Values of the coefficient of determination R^2 obtained from analysis of predicted and recorded free surface elevation time series at Portrush, Bangor and Portpatrick for 30 days starting on 12th May 2014 are 0.98, 0.99 and 0.95 respectively. These values confirm that the model is

satisfactorily validated, for C_d = 0.0025, which is therefore used for subsequent analysis. The agreement achieved with local flow conditions can be seen in the M_2 tidal amplitudes contour plot shown in Figure 5, where an amphidromic point north of Rathlin Island is identified, in agreement with previous three-dimensional numerical predictions by Davies and Jones of tidal behaviour in the Celtic and Irish Seas [39].

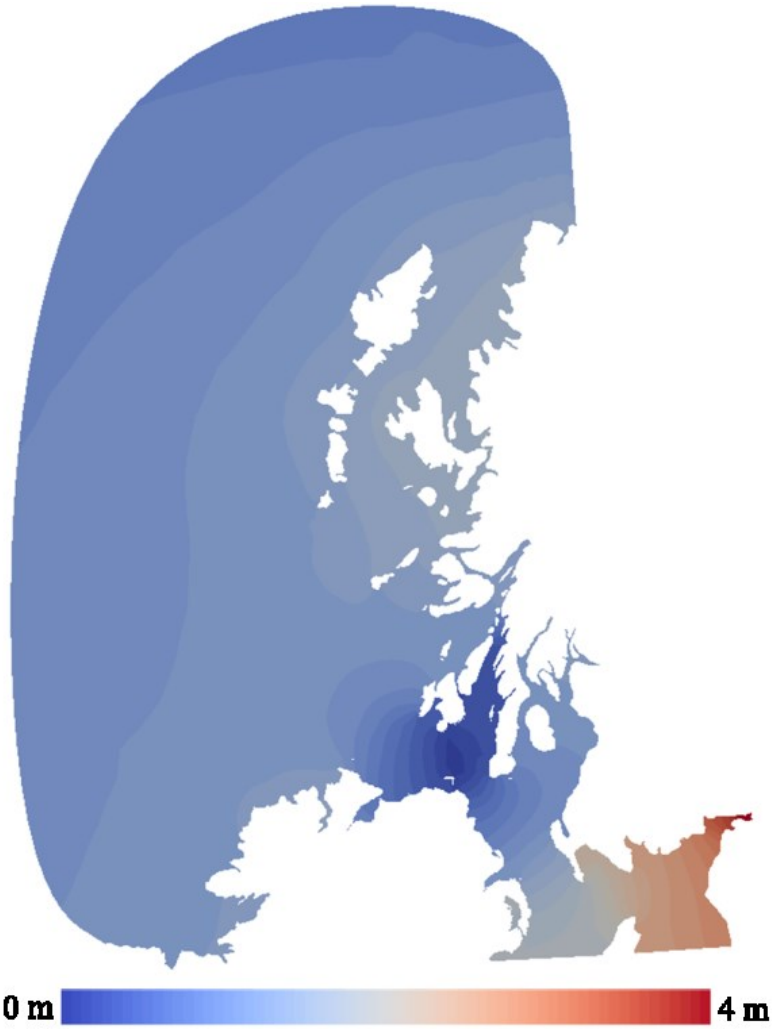

Figure 5. Numerically predicted M_2 tidal amplitudes obtained using seabed friction coefficient C_d = 0.0025.

3 Analysis

This section presents and interprets the simulations of tidal hydrodynamics in Rathlin Sound. For each case presented, the numerical model is forced at the open boundaries using solely an M_2 tidal signal, which was found to be the most energetic constituent at the site, as is also the case for other sites in the region [18]. The numerical model was run for nine M_2 tidal cycles starting on the 24th of April 2014: the first two cycles correspond to the ramp-up of the system; followed by four cycles for the spin-up of the system; the last three cycles are used in the site analysis to account for possible numerically induced small differences between cycles. The results will enable assessment of the validity of the idealised model of Pérez-Ortiz *et al*. [13] and the GC2005 analytical channel model when applied to the Rathlin Sound.

3.1 Natural state at Rathlin Sound

An accurate understanding of the natural flow dynamics in Rathlin Sound is first required to enable changes to the hydrodynamic environment caused by tidal power extraction to be assessed later. Figure 6 presents contour plots of depth-averaged flow speed and vorticity during flood, ebb and slack water. At flood tide, the coastal features of Rue Point and Fair Head constrain the flow at the exit of Rathlin Sound leading to a jet advecting south-east of Rathlin Sound. At ebb tide, the eddy generated at Rue Point advects within Rathlin Sound and constrains the westward flow, increasing flow rotationality and complicating tidal energy exploitation west of Rathlin Sound. Residual eddies are more significant at slack water from ebb to flood tide than from flood to ebb tide.

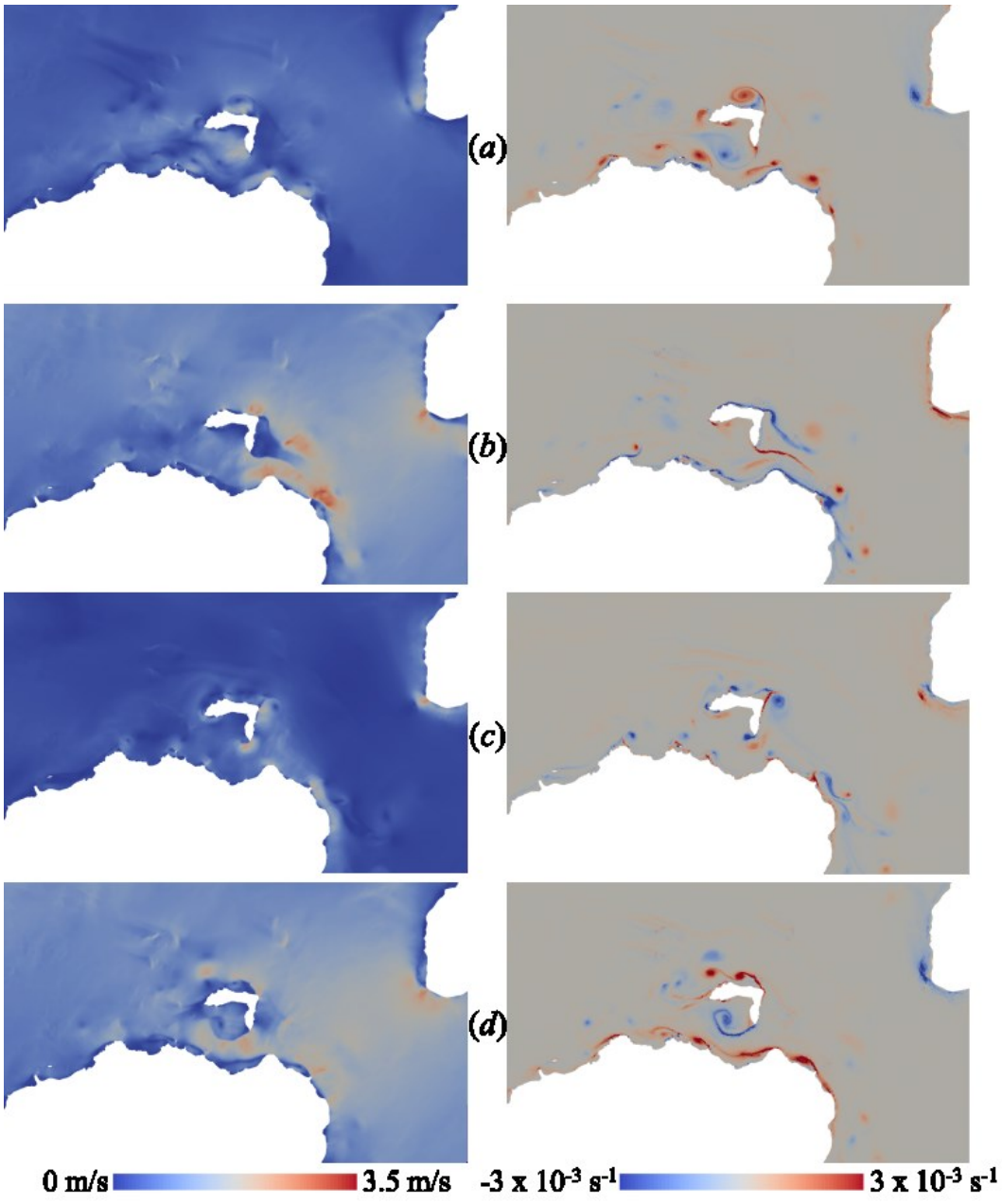

Figure 6. Numerically predicted depth-averaged flow speed (left) and vorticity (right) contour plots for undisturbed conditions at t = (*a*) slack tide, (*b*) flood tide, (*c*) slack tide and (*d*) ebb tide.

Figure 7 shows the three-tidal-cycle mean and maximum flow speed contour plots in the natural state. High velocities are predicted at the east side of Rathlin Sound, north-east of Rathlin Island, and offshore east and south-east of Rathlin Sound. The M_2 tidal signal yields mean and maximum flow speeds at the site of 2 and 3 m/s respectively. Figure 7 indicates that the most energetic region of Rathlin Sound is located at the east end, between Rue Point and Fair Head.

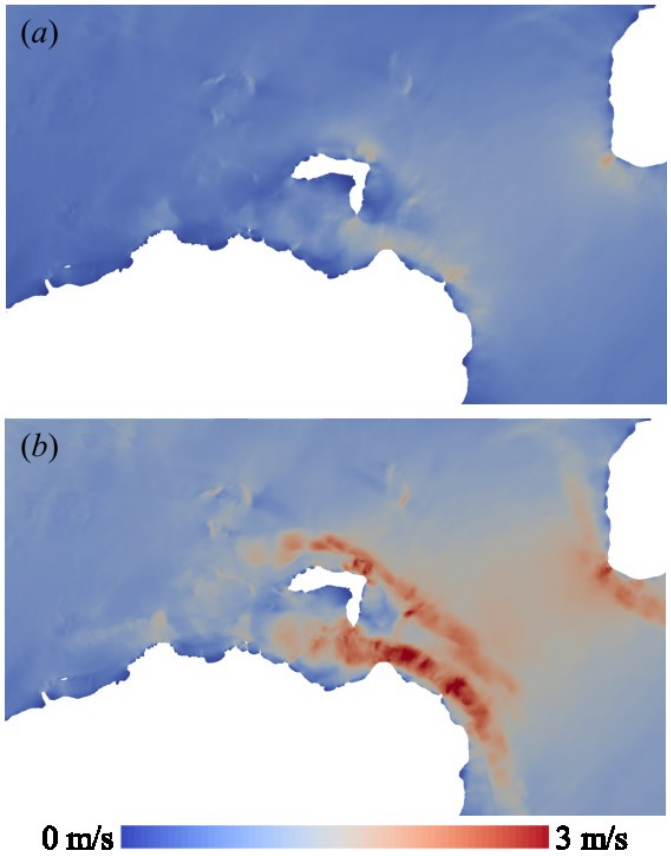

Figure 7. Contour plots of the predicted three-tidal-cycle (*a*) mean and (*b)* maximum depth-averaged flow speeds in undisturbed conditions.

3.2 Rathlin Sound resource assessment

Based on the natural state conditions shown in Figure 7, power extraction is considered east of Rathlin Sound, at the narrowest section of the strait connecting Rue Point and Fair Head, where the highest flow speeds are experienced in the strait. Power extraction is implemented over a rectangle of dimensions 100 x 4,020 m, blocking the entire strait section. A regular grid of 80 isosceles triangles is used to define the tidal array, which is inserted in the domain mesh shown in Figure 4. The extraction level in the array, k_f, is gradually increased from 0 to 3.6 (Section 2.1). It should be noted that turbine characteristics at cut-in and rated speed are not included in the present analysis (for a recent implementation see Gillibrand et al. [5]).

Figure 8 presents the three-tidal-period averaged results for: undisturbed kinetic power $\bar{P}_{ko}$, defined as the kinetic power east of Rathlin Sound with no power extraction, computed across the length of the strait as per Eq. (7); power naturally dissipated at the seabed in Rathlin Sound in the natural state $\bar{P}_s$, computed for the seabed area of the strait as shown in Eq. (8); kinetic

power east of Rathlin Sound with the tidal array present $\bar{P}_k$, computed as $\bar{P}_{ko}$; and power extracted from the flow by the tidal array $\bar{P}_e$, computed as $\bar{P}_s$ integrating solely across the array area and replacing C_d by the extraction level k_f.

$$\bar{P}_{ko} = \frac{1}{2}\int \rho h U^3 \, dL \qquad 7)$$

$$\bar{P}_S = \int \rho C_d U^3 \, dA \qquad 8)$$

Peak power extracted east of Rathlin Sound is achieved for k_f = 1.78 at 298 MW, and this limit appears not to be satisfactorily approximated by either the undisturbed kinetic power or the power naturally dissipated at the seabed in Rathlin Sound, in agreement with predictions from an idealised strait of similar geometry by Pérez-Ortiz *et al.*[13]. Furthermore, the present results show that $\bar{P}_s < \bar{P}_e < \bar{P}_{ko}$, in accordance with findings by Pérez-Ortiz *et al.* [13] when a no-slip boundary condition was applied to island and landmass and when a realistic bathymetry was implemented to define the island-landmass coastal site. Rates of decrease in $\bar{P}_k$ are similar to those observed when implementing a realistic bathymetry by Pérez-Ortiz *et al.* [13].

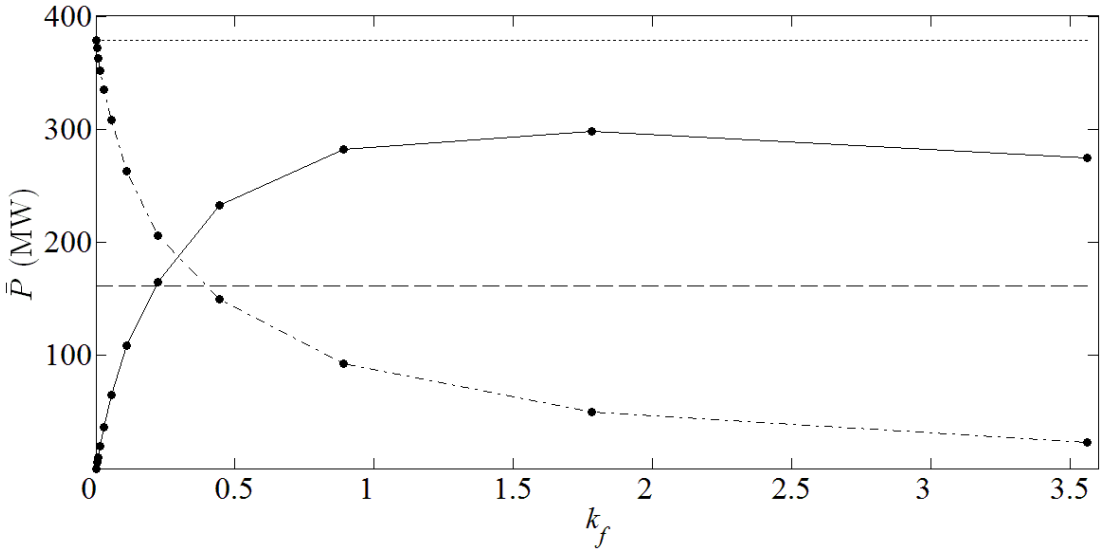

Figure 8. Power profiles as functions of k_f in Rathlin Sound: extracted power for tidal array located in the strait $\bar{P}_e$ (solid line); kinetic power for the strait with the tidal array present $\bar{P}_k$ (dash-dot line); kinetic power for undisturbed conditions in the strait $\bar{P}_{ko}$ (dotted line); and power dissipated naturally at the seabed in the strait $\bar{P}_s$ (dashed line). Markers indicate the numerically computed discrete points.

Addition of the S_2 constituent to the tidal signal increases the peak in $\bar{P}_e$ averaged over a spring-neap tidal cycle to 330 MW, which is reached when k_f = 1.78. For k_f = 1.78, addition of the remaining 6 tidal constituents N_2, K_2, K_1, O_1, P_1, and Q_1 employed for the calibration of the model in Section 2.3 reduces the peak in $\bar{P}_e$ averaged over the same spring-neap tidal cycle to 305 MW. For the two tidal signal cases, Figure 9 shows the time series of instantaneous power extracted P_e during a spring-neap tidal cycle starting on the 27th of April 2014 when k_f = 1.78.

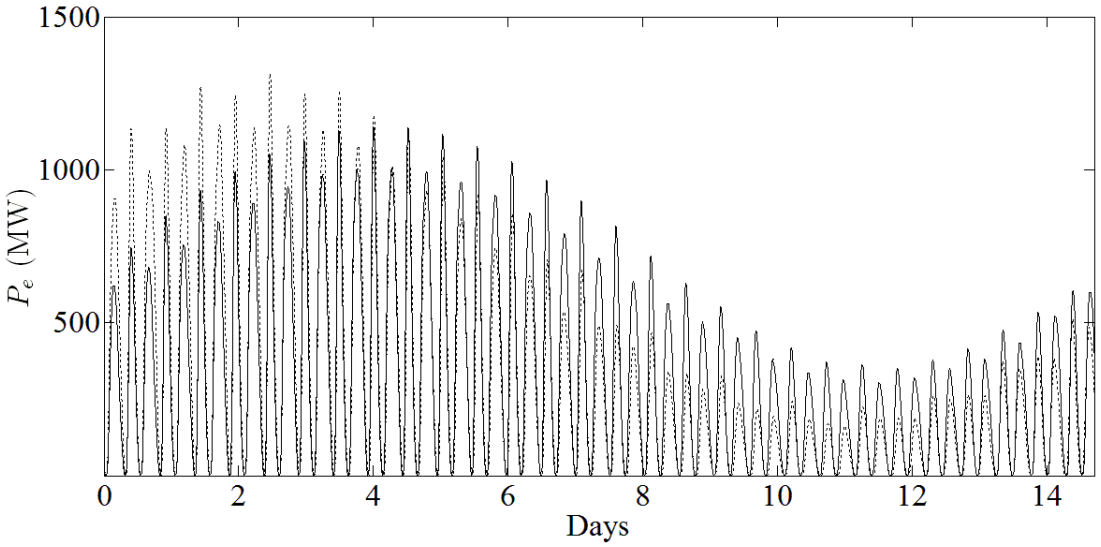

Figure 9. Instantaneous power extracted at the strait during a spring-neap tidal cycle starting on the 27th of April 2014 when k_f = 1.78, for the following driving tides: M_2+S_2 (solid line); and 8 harmonic constituents (dotted line).

Power extraction effects on the volumetric flow rate at the strait and offshore are assessed at the strait cross-section where power extraction is implemented, and at a section of equal length spanning offshore of east side of the island as per Eq. (9).

$$Q = \int hU \, dL \tag{9}$$

Figure 10 shows the volumetric flow rate in the strait and offshore, $\bar{Q}$, normalised by the volumetric flow rate in the absence of power extraction, $\bar{Q}_o$. If the difference in water depth between the strait and offshore side is accounted for, the volumetric flow rate trends obtained at both sides of the island are in agreement with those observed by Pérez-Ortiz *et al.* [13] for the realistic bathymetry case.

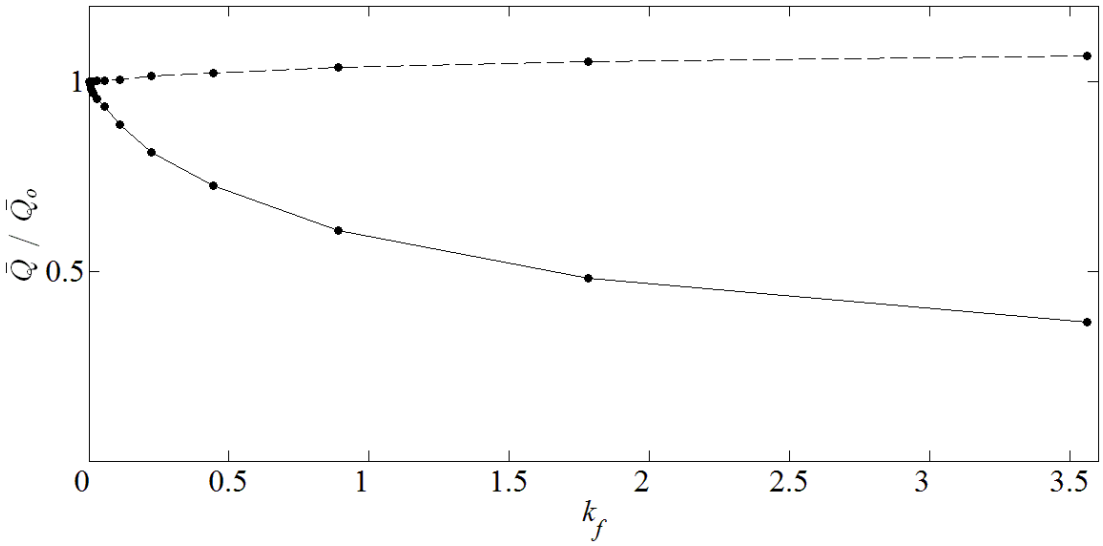

Figure 10. Changes in the ratio of actual to undisturbed volumetric flow rate across the tidal array (solid line) and through a cross-section of identical length at the offshore side of the island (dashed line). Markers indicate the numerically computed discrete points.

Comparison between Figure 8 and Figure 10 reveals that maximum power extraction in Rathlin Sound is achieved when $\bar{Q}$ through the strait reduces to approximately 48 % of $\bar{Q}_o$. This value corresponds to a higher reduction than the 57.7 % predicted by GC2005 for a channel linking two infinite ocean basins.

Figure 11 shows the cyclic behaviour of the head driving the flow assessed at the east (55.25 °N / 6.16 °W) and west (55.25 °N / 6.31 °W) of the strait with no power extraction, low extraction k_f = 0.11 and high extraction k_f = 1.78. The averaged cross-section sea surface elevations at the entrance and exit of Rathlin Sound are used to compute the head difference between the entrance and exit of the strait. Based on the amplitude of the head difference, the maximum volumetric flow rate in natural conditions and the phase difference between the peaks of head drop and volumetric flow rate, the GC2005 analytical channel model underpredicts by 51% the maximum power extracted from the numerical predictions. Changes in head difference in the strait with power extraction (Figure 11) and the existence of an alternative flow path offshore of Rathlin Island are the main reasons for the discrepancy between the analytical and numerical results. These findings are in accordance with Pérez-Ortiz *et al*. [13].

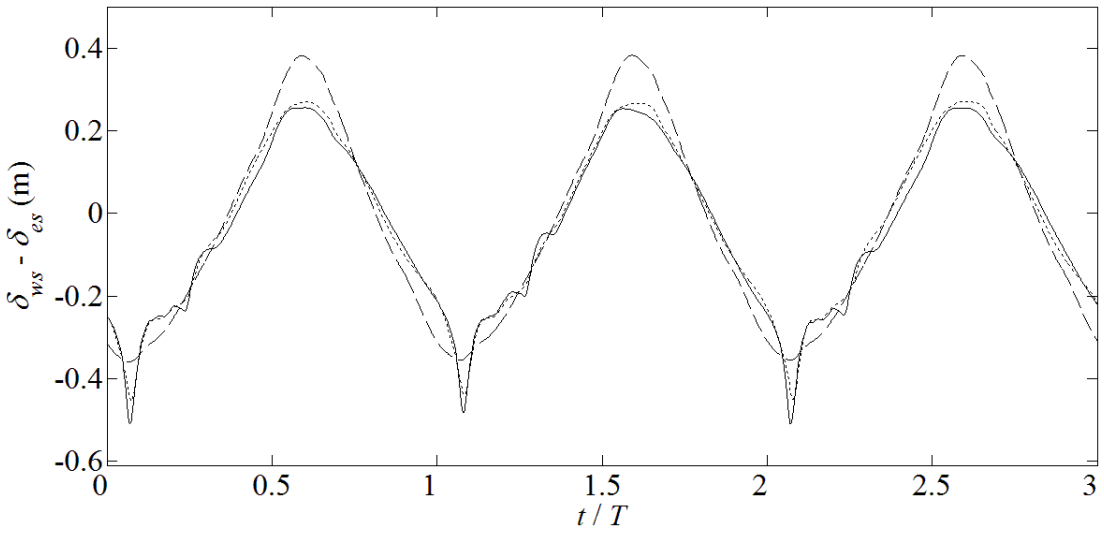

Figure 11. Flow-driving head between west and east of Rathlin Sound: no power extraction (solid line); low extraction k_f = 0.11 (dotted line); and high extraction k_f = 1.78 (dashed line).

Changes to the natural flow conditions of Rathlin Sound at maximum power extraction may not be acceptable from an environmental point of view. Figure 12 displays the spatial distribution of three-tidal-period-averaged mean flow speeds with no power extraction and at maximum power extracted east of Rathlin Sound. There is a reduction in mean flow speeds in Rathlin Sound and especially offshore east and south-east, where the jet observed in natural flood conditions is substantially diminished. Power extraction effects on flow speeds reduce further downstream, off Torr Head (see Figure 1). Changes to the site flow dynamics can be also observed in Figure 13, which includes vorticity plots at flood and ebb tides with no extraction and maximum power extracted in Rathlin Sound. Flow features advecting south-east of Rathlin Sound are reduced in magnitude at flood tide. At ebb tide, there is a weakening in eddy shedding from Rue Point and Fair Head, and flow changes are observed north of Rathlin Sound, which may be a consequence of increasing volumetric flow rates offshore of the island. Analysis of the sea surface elevation at maximum power extraction revealed three-tidal-period-averaged mean differences in the sea surface elevation at ADCP 3 of about 10 %, and of less than 1 % at Portrush and Bangor.

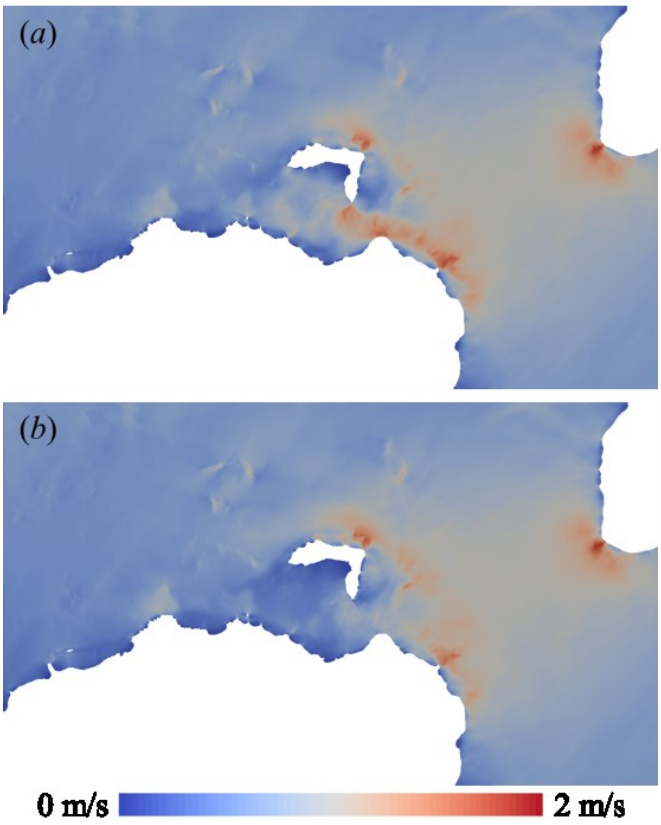

Figure 12. Contour plots of the three-tidal-cycle mean flow speeds: (*a*) no power extraction; and (*b)* extraction for k_f = 1.78.

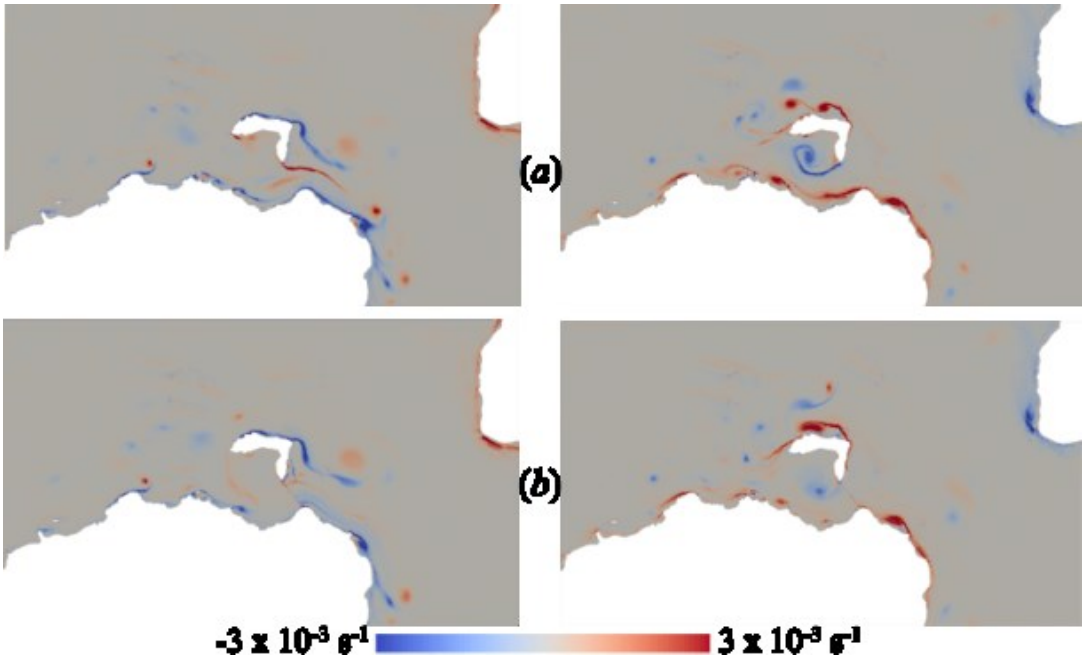

Figure 13. Vorticity contour plots with (*a*) no extraction and (*b*) k_f = 1.78 at peak flood (left) and ebb (right) tides.

Calibration of the numerical model presented in Section 2.2 was performed by altering the seabed friction coefficient, until the numerical predictions were in agreement with site

observations. However, the value chosen for the seabed friction coefficient may alter the power extraction estimates, as discussed by Adcock *et al.* [18] in an analysis of the Pentland Firth, where the available power for four rows of highly blocked turbines reduced by 15% when C_d was increased from 0.0025 to 0.005. In Rathlin Sound, when C_d is increased from 0.0025 to 0.005, the maximum power extracted is reduced by 15%, in broad agreement with Adcock *et al.* [18] and similar to the 20% reduction obtained for an idealised island-landmass coastal site by Pérez-Ortiz *et al.* [13]. The change in C_d does not appear to alter the main site flow dynamics or the level of power extraction k_f at which the peak in power extracted was reached.

3.3 Array Strait Blockage

Section 3.2 assessed the maximum power extracted in Rathlin Sound for an array blocking the entire strait cross-section. However, due to technical and environmental constraints, power extraction may be partially blocking the strait. The width of the array employed in Section 3.2 is shortened equally from both ends, to 80 % and 60 % of the original width. Figure 14 shows the three-tidal-period-averaged values of $\bar{P}_{ko}$, $\bar{P}_s$, $\bar{P}_k$ and $\bar{P}_e$ obtained for array-blockage ratios of 100 %, 80 % and 60 %, plotted against the equivalent number of turbines N_T using Eq. (5).

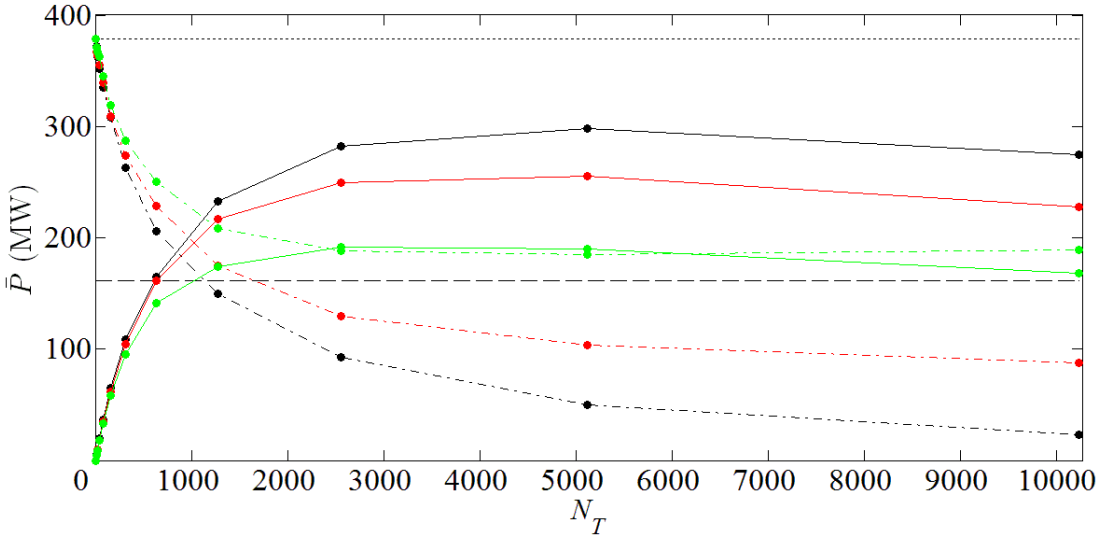

Figure 14. Power profiles as functions of the number of turbines N_T in Rathlin Sound for three blockage ratios: 100 % (black); 80 % (red); and 60 % (green). Extracted power for tidal array located in the strait $\bar{P}_e$ (solid line); kinetic power for the strait with the tidal array present $\bar{P}_k$ (dash-dot line); kinetic power for undisturbed conditions in the strait $\bar{P}_{ko}$ (dotted line); and power dissipated naturally at the seabed in the strait $\bar{P}_s$ (dashed line). Markers indicate the numerically computed discrete points.

Compared to the fully blocked case, the maximum power extracted from Rathlin Sound reduces by 14 % and 36 % for the 80 % and 60 % blockage ratios respectively. In the idealised island-landmass study by Pérez-Ortiz *et al.* [13] with a realistic bathymetry, the maximum power extracted reduced by 0.4 % and 30 % for the 80 % and 60 % blockage ratios assessed. Satisfactory agreement is obtained for the 60 % blockage ratio case between the Rathlin Sound and the idealised island-landmass coastal site. The difference observed for the 80 % blockage ratio originated from the bathymetry profile employed in the idealised study which involved a sharp reduction in water depth in the unblocked section of the strait, increasing resistance to the flow and thus limiting the bypass flow. Similar power extraction estimates are achieved for the three blockage ratios with a number of turbines in the array $N_T \leq 200$; however, the results diverge when the turbine density in the array is increased due to a reduction in the flow through the array at low blockage ratios, in agreement with Nishino and Willden [40]. Lower reduction

in kinetic power in the strait is observed when the strait blockage ratio is reduced, as the area where flow is permitted to bypass the array increases.

Changes to site flow dynamics at maximum power extraction for the three blockage ratios can be observed in the vorticity plots of Figure 15 at peak flood and ebb tides. At flood tide, as the strait blockage is reduced there is an increase in the size of vortical structures generated from the ends of the array and advecting south-east of the strait. At ebb tide, the reduction of the strait blockage ratio increases the magnitude of vortical structures advecting west of the strait – an example is the eddy generated at Rue Point which merges with other eddies generated at the north end of the array. The three-tidal-period-averaged mean flow speed in the strait bypass sections increases by 20 % and 14 % for the 80 % and 60 % blockage ratios respectively. If the seabed at the site is mobile, this local change in flow speed may accelerate sediment erosion in the bypass regions, and increase sediment deposition at the centre of the strait where mean flow speed is reduced by the presence of the tidal array. These changes in the natural sediment transport process will alter the seabed morphodynamics during the tidal-project life.

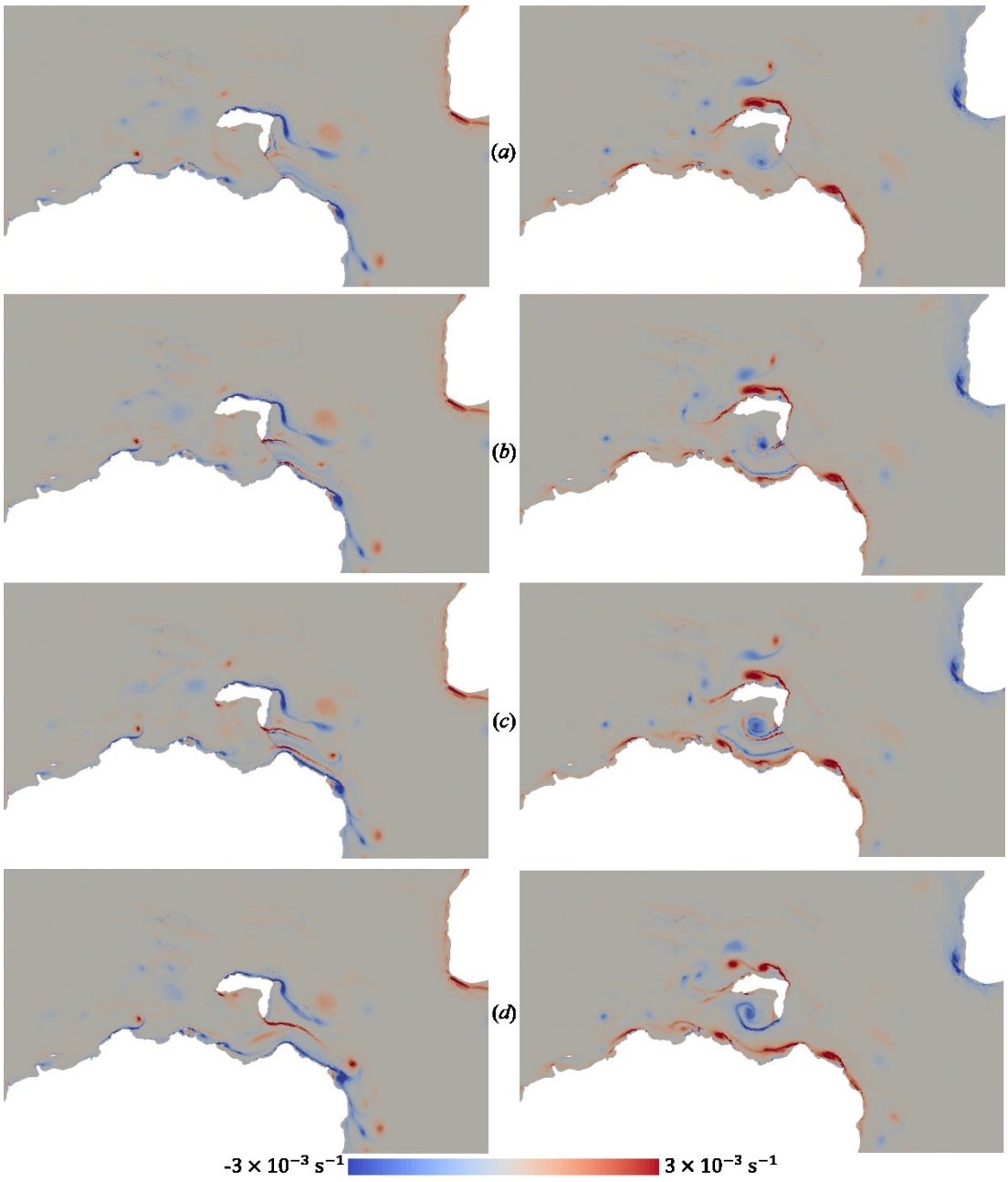

Figure 15. Vorticity contour plots at maximum power extraction for array to strait width ratios: (*a*) 100 %; (*b*) 80 %; (*c*) 60 %; and (*d*) no extraction at peak flood (left) and ebb (right) tides.

3.4 Offshore Power Extraction

The analysis of the natural state conditions in Section 3.1 indicated that high flow velocities are also achieved north-east of Rathlin Sound (Figure 7). The limits to power extraction offshore of Rathlin Sound are now assessed by considering power extraction both in the strait and offshore. Power extraction is implemented north-east of Rathlin Island over a rectangular area of the same dimensions as those of the array in the strait and extending north of the island. Figure 16 shows the dependence of the three-tidal-period-averaged values of $\bar{P}_{ko}$, $\bar{P}_s$, $\bar{P}_k$ and $\bar{P}_e$, on the power extraction level k_f when power extraction is implemented separately in the strait and offshore of the island. Maximum power extracted offshore of the island is 13 % lower than the

undisturbed kinetic power offshore of the island and 134 % higher than the extraction peak obtained in the strait.

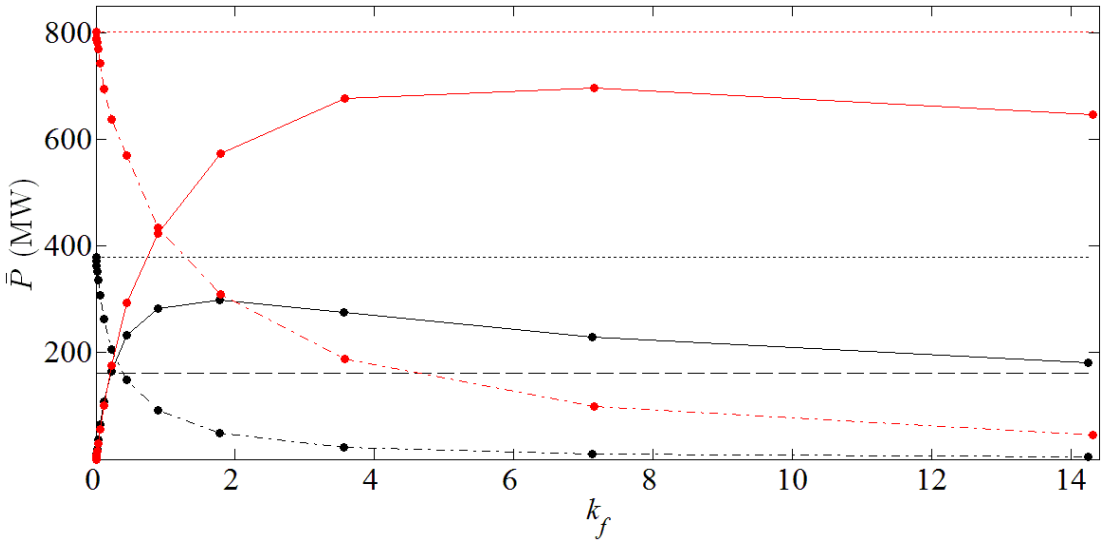

Figure 16. Power profiles as functions of k_f for the Rathlin Sound site: extraction only at strait (black) and extraction only offshore of the island (red). Extracted power for tidal array $\bar{P}_e$ (solid line); kinetic power with the tidal array present $\bar{P}_k$ (dash-dot line); kinetic power for undisturbed conditions $\bar{P}_{ko}$ (dotted line); and power dissipated naturally at the seabed $\bar{P}_s$ (dashed line). Markers indicate the numerically computed discrete points.

Changes in the natural site flow dynamics induced by the power extraction offshore of the island can be seen in the vorticity contour plots of Figure 17 at peak flood and ebb tides. The offshore array reduces the local flow which in turn prevents growth and shedding of eddies from the north-east of the island. Vortical structures are generated at the north end of the offshore array due to acceleration of the flow bypassing north of the array. Although part of the bypass flow occurs in the strait where the flow accelerates in the strait, this speed-up does not appear to alter the main flow dynamics at the strait.

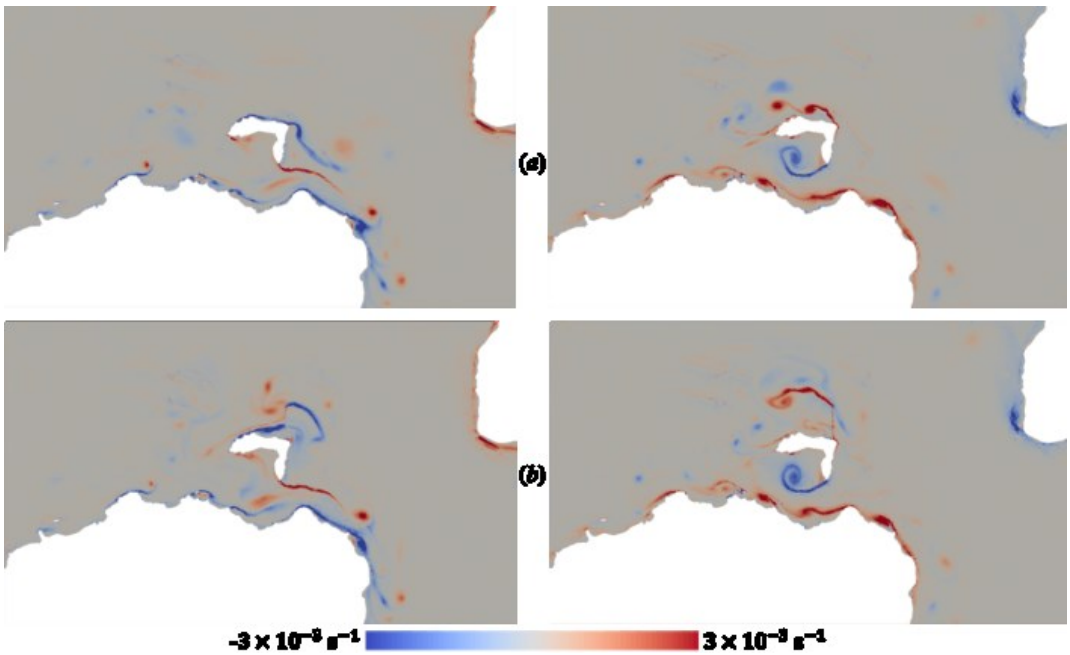

Figure 17. Vorticity contour plots with (a) no extraction and (b) k_f = 7.16 offshore of Rathlin Island at peak flood (left) and ebb (right) tides.

Table IX summarises the effects of combined power extraction in the strait and offshore of the island for seven scenarios: Scenarios 1 and2, where power is solely extracted in the strait; Scenarios 3 and 4, where power is solely extracted offshore of the island; and Scenarios 5 to 7 where power is extracted both from the strait and offshore of the island. Table IX lists the equivalent number of turbines N_T, array average power generated $\bar{P}_T$, array capacity factor CF, the average velocity $\bar{U}_o^*$, and kinetic power $\bar{P}_k^*$ deficit for each scenario. The array average power generated $\bar{P}_T$ over three tidal cycles is computed from:

$$\bar{P}_T = \frac{1}{3T}\sum_{t=1}^{3T}\sum_{i=1}^{N_T}\frac{1}{2}\rho C_P(U_i)A_T U_i^3 \qquad 10)$$

where C_P is the turbine power coefficient function (based on the turbine described in Section 3.3):

$$C_P = \begin{cases} 0 & \text{if} \quad U < U_C \\ 0.4 & \text{if} \quad U_C \le U \le U_R \\ \dfrac{2P_R}{\rho A_T U^3} & \text{if} \quad U > U_R \end{cases} \qquad 11)$$

with cut-in speed U_C of 1m/s and rated speed U_R of 2.5 m/s.

Based on $\bar{P}_T$, N_T and P_R, the capacity factor CF of the tidal farm during the three tidal cycles is computed from:

$$CF = \frac{\bar{P}_T}{N_T P_R} \qquad 12)$$

The results confirm that for the same number of turbines, higher power production rates are achieved when these are installed in the strait and offshore than solely on one side of the island. However, the increase in yield from combined extraction in strait and offshore is smaller than that observed in the idealised island-landmass study by Pérez-Ortiz *et al*. [13]. Results from Table IX indicate that at island-landmass sites, overall site power generation can be enhanced through combined power extraction. However, the results also confirm that it is necessary to analyse multiple configurations in order to maximise the site power output.

Table IX. Values of the three-tidal-period-averaged array power generated $\bar{P}_T$,, tidal array capacity factor *CF*, percentage decrease in mean strait velocity $\bar{U}_o^*$ and percentage decrease in mean kinetic power$\bar{P}_k^*$ according to equivalent numbers of turbines N_T in the strait (S) and offshore side (O) of Rathlin Island.

Scenario	Island Side	N_T	$\bar{P}_T$ [MW]	*CF* [%]	$\bar{U}_o^*$ [%]	$\bar{P}_k^*$ [%]
1	S	160	27.9	17.5	-9.4	-18.6
	O	0	n.a.	n.a.	+0.4	+2.1
2	S	320	46.1	14.4	-14.9	-30.5
	O	0	n.a.	n.a.	+0.7	+3.2
3	S	0	n.a.	n.a.	+1.7	+2.8
	O	160	23.9	14.9	-5.2	-7.5
4	S	0	n.a.	n.a.	+2.9	+4.4
	O	320	43.2	13.5	-7.6	-13.4
5	S	80	15.7	19.6	-5.8	-10.4
	O	80	12.7	15.8	-2.7	-3.2
6	S	160	28.7	18	-8	-16.5
	O	160	24.1	15.1	-4.7	-6.1
7	S	320	47.8	14.9	-13.2	-28.3
	O	320	44	13.8	-7.1	-10.4

4 Conclusion

Shallow flow simulations have been used to estimate the maximum power extracted in the Rathlin Sound under M_2 tidal forcing. Close agreement was obtained between model predictions and field measurements of tidal parameters for a uniform value of seabed friction coefficient C_d = 0.0025. Model results were compared against the GC2005 analytical solution for a channel linking two infinite ocean basins, and numerical predictions assuming an idealised island-landmass coastal site by Pérez-Ortiz *et al*. [13]. The shallow flow model predicted averaged and maximum undisturbed flow speeds of 2 and 3 m/s within Rathlin Sound. Maximum power extracted at the east section of the Rathlin Sound was found to be 298 MW, which was quite different to the undisturbed kinetic power or the power dissipated naturally at the seabed. When an S_2 constituent was added to the tidal signal, the maximum power extracted increased to 330 MW. Predicted trends in volumetric flow ratios through the strait and offshore of the island were in agreement with those previously obtained for an idealised island-landmass coastal site. The GC2005 analytical channel model, based on the head drop along the strait computed from transect-averaged free surface elevations, gave a power-extracted prediction that was lower by 51 % than that from the present shallow flow model – a similar result was

also obtained in the equivalent idealised island-landmass study. Primary reasons for discrepancies between the analytical and numerical predictions were found to be the increase of driving head with power extraction in the strait and the availability of an alternative flow path offshore of Rathlin Island. At maximum power extraction, the flow dynamics at Rathlin Sound altered, with the speed reducing substantially in the strait and south-east of the site, and mean differences in sea surface elevation of 10 % and less than 1 % predicted respectively east of the site and in the far-field. When C_d was doubled from 0.0025 to 0.005 the maximum power extracted reduced by 15%, in broad agreement with the 20 % decrease found in the idealised island-landmass study. This again highlights the importance in the choice of value of bed friction coefficient used here to tune the model during calibration because of its effect on the end results. The maximum power extracted was also found to be sensitive to the strait blockage ratio, with the maximum power reducing by 14 % and 36 % for 80 % and 60 % blockage respectively, in comparison to 100 % blockage. This decrease in maximum power extracted as the blockage ratio reduced was in broad agreement with findings of the previous idealised island-landmass study [13]. The discrepancies observed for the 80 % blockage ratio case may have been due to the rapid reduction in water depth in the strait bypass regions of the idealised island-landmass study. Increases in the average flow speed at the bypass strait sections of 20 % and 14 % were found for 80 % and 60 % blockage ratios, which could lead to seabed erosion at strait bypass sections. Offshore power extraction was also assessed north-east of Rathlin Island, where high flow speeds were identified in natural conditions. Maximum power extracted offshore of the island was 134 % higher than the maximum power extracted in the strait. At maximum power extracted, the offshore coastal flow dynamics were modified, whereas the hydrodynamics of the strait were not significantly altered. Results showed that implementation of power extraction both in strait and offshore yielded higher power generation rates than extraction solely in the strait or offshore of the island (for equivalent number of turbines). Nevertheless, this increase in power extraction was lower than that observed in the idealised island-landmass study. The present study confirms that Rathlin Sound has considerable potential for exploitation as a source of tidal stream power. Further research is required in order to optimise tidal power extraction at this complicated site.

The authors intend to investigate impacts on the environment at levels of power extraction below maximum, to provide information for site developers when evaluating potential array size. To improve the accurate representation of turbines in the model, it is recommended that the increased bed friction approach used in the present shallow flow model be replaced by a more advanced methodology, such as linear momentum actuator disc theory (LMADT) (see Houlsby *et al.* [41]) that accounts for local blockage, bypass flow and mixing losses. With the availability of greater computer power, three-dimensional modelling is also recommended, following the approaches taken by Roc *et al*. [42] and O'Hara Murray and Gallego [43].

Acknowledgements

The authors would like to thank GE Renewable Energy for their support, and the Applied Modelling and Computation Group at Imperial College of London for advice and free access to the software Fluidity. The authors would like to thank DP Marine Energy for providing the ADP data. The authors would also like to thank Paul Vigars, Dr. Helen Smith and Dr. Qing Xiao who have provided valuable insight. This work was supported with funding from the ETI and the EPSRC through the Industrial Doctoral Centre for Offshore Renewable Energy (EP/J500847/1).

References

[1] Intergovernmental Panel on Climate Change, “Climate change 2001: Synthesis summary,” 2001.

[2] M. Tsoskounoglou, G. Ayerides, and E. Tritopoulou, “The end of cheap oil: Current status and prospects,” *Energy Policy*, vol. 36, no. 10, pp. 3797–3806, Oct. 2008.

[3] M. Lewis, S. P. Neill, P. E. Robins, and M. R. Hashemi, “Resource assessment for future generations of tidal-stream energy arrays,” *Energy*, vol. 83, pp. 403–415, Apr. 2015.

[4] M. J. Lewis, A. Angeloudis, P. E. Robins, P. S. Evans, and S. P. Neill, “In fl uence of storm surge on tidal range energy,” *Energy*, vol. 122, pp. 25–36, 2017.

[5] P. Gillibrand, R. Walters, and J. McIlvenny, “Numerical simulations of the effects of a tidal turbine array on near-bed velocity and local bed shear stress,” *Energies*, vol. 9, no. 10, p. 852, Oct. 2016.

[6] M. J. Lewis, S. P. Neill, M. R. Hashemi, and M. Reza, “Realistic wave conditions and their influence on quantifying the tidal stream energy resource,” *Appl. Energy*, vol. 136, pp. 495–508, Dec. 2014.

[7] M. R. Hashemi, S. P. Neill, P. E. Robins, A. G. Davies, and M. J. Lewis, “Effect of waves on the tidal energy resource at a planned tidal stream array,” *Renew. Energy*, vol. 75, pp. 626–639, Mar. 2015.

[8] M. S. Horritt, “A linearized approach to flow resistance uncertainty in a 2-D finite volume model of flood flow,” *J. Hydrol.*, vol. 316, no. 1–4, pp. 13–27, Jan. 2006.

[9] C. Garrett and P. Cummins, “The power potential of tidal currents in channels,” *Proc. R. Soc. A Math. Phys. Eng. Sci.*, vol. 461, no. 2060, pp. 2563–2572, Aug. 2005.

[10] S. Draper, A. G. L. Borthwick, and G. T. Houlsby, “Energy potential of a tidal fence deployed near a coastal headland,” *Philos. Trans. R. Soc. A Math. Phys. Eng. Sci.*, vol. 371, no. January, 2013.

[11] S. Draper, T. A. A. Adcock, A. G. L. Borthwick, and G. T. Houlsby, “Estimate of the tidal stream power resource of the Pentland Firth,” *Renew. Energy*, vol. 63, pp. 650–657, Mar. 2014.

[12] S. Draper, “Tidal stream energy extraction in coastal basins,” Doctoral Thesis, University of Oxford, Oxford, United Kingdom, 2011.

[13] A. Pérez-Ortiz, A. G. L. Borthwick, J. McNaughton, H. C. M. Smith, and Q. Xiao, “Resource characterization of sites in the vicinity of an island near a landmass,” *Renew. Energy*, vol. 103, pp. 265–276, Apr. 2017.

[14] A. Pérez-Ortiz, A. G. L. Borthwick, H. Smith, P. Vigars, and Q. Xiao, “Tidal Resource in Strait between Island and Landmass,” in *Proceedings of the 11th European Wave and Tidal Energy Conference*, 2015, pp. 1–10.

[15] G. Sutherland, M. Foreman, and C. Garrett, “Tidal current energy assessment for Johnstone Strait, Vancouver Island,” *Proc. Inst. Mech. Eng. Part A J. Power Energy*, vol. 221, no. 2, pp. 147–157, Jan. 2007.

[16] R. H. Karsten, J. M. McMillan, M. J. Lickley, and R. D. Haynes, “Assessment of tidal current energy in the Minas Passage, Bay of Fundy,” *Proc. Inst. Mech. Eng. Part A J. Power Energy*, vol. 222, no. 5, pp. 493–507, Aug. 2008.

[17] Black & Veatch Consulting Ltd, “UK tidal current resource & economics : Appendix C,” 2011.

[18] T. A. A. Adcock, S. Draper, G. T. Houlsby, A. G. L. Borthwick, and S. Serhadlıoğlu, “The available power from tidal stream turbines in the Pentland Firth,” *Proc. R. Soc. A Math. Phys. Eng. Sci*, vol. 469, 2013.

[19] F. O’Rourke, F. Boyle, and A. Reynolds, “Tidal current energy resource assessment in Ireland: Current status and future update,” *Renew. Sustain. Energy Rev.*, vol. 14, no. 9, pp. 3206–3212, Dec. 2010.

[20] “Edina Digimap Service. Hydrospatial one, gridded bathymetry. 2014.,” 2015. [Online]. Available: http://edina.ac.uk/digimap/.

[21] C. J. Cotter, D. A. Ham, and C. C. Pain, “A mixed discontinuous/continuous finite element pair for shallow-water ocean modelling,” *Ocean Model.*, vol. 26, no. 1–2, pp. 86–90, Jan. 2009.

[22] “Fluidity Manual,” Applied Modelling and Computation Group, Department of Earth Science and Engineering, South Kensington Campus, Imperial College London, London, United Kingdom, Version 4.1.10, 2014.

[23] R. Martin-Short, J. Hill, S. C. Kramer, A. Avdis, P. A. Allison, and M. D. Piggott, “Tidal resource extraction in the Pentland Firth, UK: Potential impacts on flow regime and sediment transport in the Inner Sound of Stroma,” *Renew. Energy*, vol. 76, pp. 596–607, Apr. 2015.

[24] J. Donea and A. Huerta, *Finite element methods for flow problems*. Chichester, UK: John Wiley & Sons, Ltd, 2003, p. 350.

[25] W. Rodi, *Turbulence Models and their Appliation in Hydraulics*, 2nd ed. International Association for Hydraulic Research, Delft, The Netherlands, 1984.

[26] D. R. Plew and C. L. Stevens, “Numerical modelling of the effect of turbines on currents in a tidal channel – Tory Channel, New Zealand,” *Renew. Energy*, vol. 57, pp. 269–282, Sep. 2013.

[27] R. Vennell, S. W. Funke, S. Draper, C. Stevens, and T. Divett, “Designing large arrays of tidal turbines: A synthesis and review,” *Renew. Sustain. Energy Rev.*, vol. 41, pp. 454–472, Jan. 2015.

[28] T. A. A. Adcock, A. G. L. Borthwick, and G. T. Houlsby, “The open boundary problem in tidal basin modelling with energy extraction,” in *Proceedings of the 9th European Wave and Tidal Energy Conference*, 2011, pp. 1–7.

[29] J. C. Iliffe, M. K. Ziebart, J. F. Turner, A. J. Talbot, and A. P. Lessnoff, "Accuracy of vertical datum surfaces in coastal and offshore zones," *Surv. Rev.*, vol. 45, no. 331, pp. 254–262, Jul. 2013.

[30] G. D. Egbert and L. Erofeeva, "OSU Tidal Data Inversion." [Online]. Available: http://volkov.oce.orst.edu/tides/. [Accessed: 05-Feb-2013].

[31] "QGIS Geographic Information System," *QGIS Development Team. Open Source Geospatial Foundation Project.*, 2015. [Online]. Available: http://qgis.osgeo.org.

[32] C. Geuzaine and J. Remacle, "Gmsh: A 3D finite element mesh generator with built-in pre- and post- processing facilities," *Int. J. Numer. Methods Eng.*, vol. 0, pp. 1–24, 2009.

[33] A. Avdis, A. S. Candy, J. Hill, S. C. Kramer, and M. D. Piggott, "Efficient unstructured mesh generation for marine renewable energy applications." Renewable Energy, submitted, 2017.

[34] J. Lambrechts, R. Comblen, V. Legat, C. Geuzaine, and J.-F. Remacle, "Multiscale mesh generation on the sphere," *Ocean Dyn.*, vol. 58, no. 5, pp. 461–473, 2008.

[35] DP Marine Energy Ltd, "Fairhead Tidal ADCP Campaign." Personal communication, 2014.

[36] British Oceanographic Data Centre, "UK Tidal Gauge Network," 2015. [Online]. Available: https://www.bodc.ac.uk/data/online_delivery/ntslf/. [Accessed: 10-Jul-2015].

[37] S. Baston and R. Harris, "Modelling the hydrodynamic characteristics of tidal flow in the Pentland Firth," in *9th European Wave and Tidal Energy Conference*, 2011, p. 7.

[38] R. Pawlowicz, B. Beardsley, and S. Lentz, "Classical tidal harmonic analysis including error estimates in MATLAB using T_TIDE," *Comput. Geosci.*, vol. 28, no. 8, pp. 929–937, Oct. 2002.

[39] A. M. Davies and J. E. Jones, "A three dimensional model of the M2, S2, N2, K1 and O1 tides in the Celtic and Irish Seas," *Prog. Ocean.*, vol. 29, pp. 197–234, 1992.

[40] T. Nishino and R. H. J. Willden, "The efficiency of an array of tidal turbines partially blocking a wide channel," *J. Fluid Mech.*, pp. 1–11, Aug. 2012.

[41] G. Houlsby, S. Draper, and M. L. G. Oldfield, "Application of linear momentum actuator disc theory to open channel flow," *Tech. Rep. 2296-08, OUEL*, 2008.

[42] T. Roc, D. C. Conley, and D. Greaves, "Methodology for tidal turbine representation in ocean circulation model," *Renew. Energy*, vol. 51, pp. 448–464, Mar. 2013.

[43] R. O'Hara Murray and A. Gallego, "A modelling study of the tidal stream resource of the Pentland Firth, Scotland," *Renew. Energy*, vol. 102, pp. 326–340, Mar. 2017.